

SVR Algorithm as a Tool for More Optimal Intergalactic Medium Simulation in the Epoch of Reionization

MAHSA BERAHMAN,^{1,2} SEYED SAJAD TABASI,^{3,2} JAVAD T. FIROUZJAEI,^{1,2,4} AND S. MOBINA HOSSEINI^{1,2}

¹*Department of Physics, K.N. Toosi University of Technology, P.O. Box 15875-4416, Tehran, Iran*

²*PDAT Laboratory, Department of Physics, K. N. Toosi University of Technology, P.O. Box 15875-4416, Tehran, Iran*

³*Department of Physics, Sharif University of Technology, P. O. Box 11155-9161, Tehran, Iran*

⁴*School of Physics, Institute for Research in Fundamental Sciences (IPM), P. O. Box 19395-5531, Tehran, Iran*

ABSTRACT

All kinds of simulations of the intergalactic medium, such as hydrodynamic simulation, N-body simulation, numerical and semi-numerical simulation, etc., have been used to realize the history of this medium. In addition, emulators also have become widely used in recent years. Especially because they are very fast, they are used in many works instead of actual complete simulations. Emulators are trained with the help of simulator results and can work with very high accuracy similar to real simulators. Usually, reliable machine learning algorithms, such as neural networks, are used to program these emulators. In this work, we show that one of the best machine learning algorithms that can be used in general and have extremely high accuracy is the Support Vector Regression algorithm. This algorithm works better than the Multilayer Perceptron algorithm not only from the practical point of view but also from the theoretical point of view. To prove this issue, we have considered the 21SSD hydrodynamical simulation in addition to the theoretical arguments, and we have used both algorithms to be trained by this simulation for comparison. Finally, we have shown that the Support Vector Regression algorithm can be a much better and more accurate algorithm than neural network algorithms in future emulations, and by mastering it, one can neglect other algorithms with full confidence. Although this work is focused only on an intergalactic medium simulation in the Epoch of Reionization, it can be used for all other simulations regardless of their type. In other words, it can be employed for all hydrodynamic simulations, N-body simulations, etc. in all cosmic epochs and rely on its results.

Unified Astronomy Thesaurus concepts: Intergalactic medium (813); H I line emission (690); Reionization (1383)

1. INTRODUCTION

Almost a decade after the prediction of the 21-cm line as a tool for probing neutral hydrogen atoms in space, the first detection of this line using a radio telescope marked a turning point in astrophysics by opening new avenues for exploring the cosmos (Van de Hulst 1945; Ewen & Purcell 1951). The 21-cm line corresponds to the wavelength of the hyperfine transition between the singlet and triplet states of neutral hydrogen atoms in their ground state. Although this transition is difficult to be observed in laboratory conditions, it

is detectable in astronomical phenomena because neutral hydrogen exists in sufficient quantities (Furlanetto et al. 2006; Moazzenzadeh & Firouzjaee 2021). The 21-cm data can be used to map large-scale structures (LSS) and test cosmological theories. While the cosmic microwave background (CMB) data have provided valuable information about the early and late universe, many questions have remained unanswered in $z \sim 1100$ to $z \sim 3$. The Thompson scattering effects on the CMB photons and observations of high-redshift quasars (Fan et al. 2006; Jiang et al. 2016), galaxies (Chen et al. 2007), and gamma-ray burst (Totani et al. 2006) shed light on the evolution of the universe during the Epoch of Reionization (EoR). In order to comprehend the formation of the first stars and galaxies, we need to acquire 21-cm data from the end of the recombination to the EoR (Furlanetto et al. 2006; Shaver et al. 1999).

It was incredibly challenging to distinguish the neutral hydrogen signal from the galactic synchrotron radiation and ex-

mahsa.brahman72@gmail.com

[sstabasi98@gmail.com](mailto:ssstabasi98@gmail.com)

firozjaee@kntu.ac.ir

mobinahosseini954@gmail.com

tragalactic foreground signals, which can be up to 5 times brighter (Dillon et al. 2014; Pober et al. 2013), and it was detected for the first time by Experiment to Detect the Global EoR Signature (EDGES; Bowman et al. 2018). For this reason, facilities currently in operation, including LOw Frequency ARray (LOFAR; van Haarlem et al. 2013), Murchison Widefield Array (MWA; Tingay et al. 2013), Giant Metrewave Radio Telescope (GMRT; Paciga et al. 2013), and Hydrogen Epoch of Reionization Array (HERA; Neben et al.), focus on gaining statistical data, such as power spectra, with the advantage of much better signal-to-noise ratios. Since each of the mentioned interferometers has an upper limit in respective redshifts, future research requires new evolving methods for obtaining astrophysical data.

Considering that the 21-cm signal depends on cosmological and astrophysical processes that are even unknown in some cases, one of the challenges in this field is the construction of mock samples. Many endeavors have been made to simulate the expected signals that image the EoR over a redshift range between 27 and 6. These signals depend on various astrophysical parameters, such as gas density, ionization fraction, kinetic temperature, and local $Ly\alpha$ flux.

Cosmological simulations are essential for understanding the EoR and help to guide observational efforts to detect the 21-cm signal from the early universe. They have also provided valuable insights into the formation and evolution of cosmic structures and the physical processes that govern their development. For instance, 21cmFAST and SimFast21 simulations have been generated for computing the 21-cm signal without using 3D radiative simulations (Santos et al. 2010). Hosseini et al. (2023) used the 21cmFAST simulation to compare the observational data of the neutral hydrogen fraction with models obtained from the simulation and constrained some important characteristics of the IGM during the EoR. The study revealed that the fraction of the galactic gas in stars for 10^7 solar mass minihalos and the escape fraction (proportion of ionizing photons that escape into the IGM) should be less than 0.5 to achieve the best possible alignment with the observational data. Mesinger et al. (2011) employed a combination of the Markov Chain Monte Carlo (MCMC) method and the 21cmFAST semi-numerical code to conduct a large-scale simulation of Cosmic Dawn and the EoR. Kern et al. (2017) demonstrated productive efforts by using the MCMC framework to include an emulator that enables Bayesian parameter constraints across a range of model parameters.

Schmit & Pritchard (2018) used neural networks to address the issue of the cost of using Bayesian parameters and simulate the power spectrum. Chardin et al. (2019) introduced Cosmological Reionization and Deep Learning (CRADLE), an autoencoder convolutional neural network (CNNs) that used two-dimensional maps of the star and gas density

and described 3D maps of the intergalactic medium (IGM) in the EoR. Moreover, the 21SSD simulation is a database of possible signals publicly available at 21ssd.obspm.fr that uses hydrodynamic simulations in 3D space to avoid irrelevant calculations. The 21SSD simulation covers the EoR between redshifts 15 and 6. The simulation incorporates radiative hydrodynamics and accounts for fluctuations in heating and Wouthuysen-Field coupling through the utilization of X-ray and Lyman line transfer (Semelin et al. 2017).

In this paper, we present the general equations governing the physics of hydrogens in the IGM in §2, discuss the significance of the EoR in §3, and explain the 21SSD simulation and its free parameters in §4. The machine learning (ML) methods used in this paper, specifically multilayer perceptron (MLP) and support vector regression (SVR) algorithms, are described in §5. §6 focuses on evaluating the accuracy and correctness of the results obtained from the MLP and SVR methods. The analysis also involves comparing the outputs generated by these methods with the 21SSD outcomes. In §7, the advantages of employing these algorithms for estimating crucial astrophysical and cosmological parameters of the IGM are discussed.

2. GENERAL EQUATIONS

In this section, we review fundamental definitions and general equations that are essential for understanding the physics of the 21-cm signal. The 21-cm signal is the spectral lines of neutral hydrogen resulting from the interaction of the proton magnetic moment and the ground state electron. T_s is the spin temperature of the gas that is defined as the ratio between the number density of the singlet and triplet states of the hydrogen in the ground state which follows the Boltzmann equation

$$\frac{n_1}{n_0} = \frac{g_1}{g_0} \exp(-T_*/T_s), \quad (1)$$

where $T_* \equiv hc/k_B\lambda_{21cm} = 0.068K$, h is the dimensionless Hubble constant, c represents the speed of light, $k_B \approx 1.38 \times 10^{-23} J.K^{-1}$ is the Boltzmann constant, and $(g_1/g_0) = 3$ is the ratio of the statistical degeneracy factors of the two states (Field 1958). The optical depth of the IGM for the 21-cm signal incorporates various physical parameters, including the neutral hydrogen fraction, the hydrogen comoving number density, the spin temperature, and the peculiar velocity along the line of sight, which is given by

$$\tau = \frac{3c^3 \hbar A_{10} x_{HI} n_H}{16k_B T_s \nu_0^2} \frac{1}{H(z) + (1+z)\partial_r \nu_r}, \quad (2)$$

where \hbar is the reduced Planck constant, $A_{10} = 2.85 \times 10^{-15} s^{-1}$ is the Einstein spontaneous emission rate coefficient (Field 1958), x_{HI} denotes the neutral fraction of hydrogen, n_H is the hydrogen comoving number density, $\nu_0 = 1420.4$ MHz is the

rest-frame frequency of the 21-cm signal, $H(z)$ is the Hubble parameter, and $\partial_r v_r$ is the comoving gradient of the peculiar velocity along the line of sight (Field 1959).

The brightness temperature, T_b , is commonly used to measure the apparent temperature of an object based on its observed specific intensity. In the case of the CMB, it closely resembles the spectrum of a blackbody and exhibits an approximate temperature of $2.73(1+z)K$. Since it is substantially greater than T_* , the Rayleigh-Jeans approximation can also be used to estimate it. As a result, we may write the brightness temperature at $z = \nu_0/\nu_{obs} - 1$ as follows (Furlanetto et al. 2006)

$$T_b = T_s(1 - e^{-\tau}) + T_{CMB}e^{-\tau}, \quad (3)$$

where T_{CMB} is the CMB temperature. In Eq.3, the first term corresponds to the component originating from the 21-cm signal, capturing its inherent characteristics. This term quantifies the contribution of the neutral hydrogen distribution and its corresponding temperature fluctuations. On the other hand, the second term accounts for the influence of the CMB radiation on the observed brightness temperature. It represents the impact of the CMB, which pervades the universe and contributes to the overall measured intensity alongside the 21-cm signal. The difference in brightness temperature between the 21-cm line and the CMB is an important quantity for studying the EoR, as it provides a way to map the distribution of neutral hydrogen in the IGM at different redshifts. A common way to express the difference in brightness temperature between the 21-cm line and the CMB is (Furlanetto et al. 2006)

$$\begin{aligned} \delta T_b &= \frac{T_s - T_{CMB}}{1+z}(1 + e^{-\tau}) \\ &= 27x_{HI}(1 - \frac{T_{CMB}}{T_s})(\frac{0.15}{\Omega_m} \frac{1+z}{10})^{\frac{1}{2}}(\frac{\Omega_b h}{0.023})mK, \end{aligned} \quad (4)$$

where $\Omega_m = 0.315$ and $\Omega_b = 0.0484$ denote the fractional energy content of matter and baryonic matter, respectively. Three factors affect the spin temperature of the 21-cm line: i) CMB photons absorption, ii) Collisions with other hydrogen atoms, free electrons, and protons, and iii) UV photons scattering. The spin temperature is affected by an equilibrium between excitation and de-excitation as

$$\begin{aligned} n_1(C_{10} + P_{10} + A_{10} + B_{10}I_{CMB}) \\ = n_0(C_{01} + P_{01} + A_{01} + B_{01}I_{CMB}) \end{aligned}, \quad (5)$$

where B_{10} and $B_{01} = 3B_{10}$ are the Einstein coefficients, C_{01} and P_{01} (C_{10} and P_{10}) are excitation (de-excitation) rates from collisions and UV scattering. Additionally, $I_{CMB} = 2\nu_{21}^2 k_B T_{CMB}/c^2$ is the energy flux of CMB photons, and $A_{01} = 2h\nu_{21}^3 c^{-2} B_{10}$ indicates spontaneous emission rate. According to Eq.5, the spin temperature can be rewritten as Eq.6

based on the mentioned three effective processes

$$T_s^{-1} = \frac{T_\gamma^{-1} + x_\alpha T_\alpha^{-1} + x_c T_k^{-1}}{1 + x_\alpha + x_c}. \quad (6)$$

Here, T_γ refers to the temperature of the background photons, which is commonly determined by the CMB, so $T_\gamma = T_{CMB}$. T_k and T_α are the kinetic temperature of the gas and $Ly\alpha$ temperature. Ultimately, $x_\alpha \equiv P_{10}T_*/A_{10}T_\gamma$ and $x_c \equiv C_{10}T_*/A_{10}T_\gamma$ are coupling coefficients for the $Ly\alpha$ and collisions scattering. When collisions and $Ly\alpha$ are efficient, the spin temperature is independent of the CMB and follows one of the T_k and T_α . More specifically, particle collisions take one of the following forms: hydrogen-hydrogen, hydrogen-electron, and hydrogen-proton. Therefore, x_c can be calculated as follows

$$\begin{aligned} x_c &= x_c^{HH} + x_c^{eH} + x_c^{pH} \\ &= \frac{T_*}{A_{10}T_\gamma} [k_{10}^{HH}(T_k)n_H + k_{10}^{eH}(T_k)n_e + k_{10}^{pH}(T_k)n_p], \end{aligned} \quad (7)$$

where k_{10}^{HH} , k_{10}^{eH} , and k_{10}^{pH} are rate coefficients of the three collision forms. n_p and n_e are the number densities of proton and electron in the IGM.

3. THE EPOCH OF REIONIZATION

The emergence of the first galaxies several hundred million years after the Big Bang marked a critical juncture in the evolution of the universe. This transition involved a shift from a simple and homogeneous state to a more complex and structured one (Barkana & Loeb 2001). During the formation of the first stars, composed primarily of pure hydrogen and helium without heavy elements (zero metallicity), and the subsequent formation of second-generation stars containing small amounts of heavy elements, ultraviolet photons ionized the neutral hydrogen gas in the IGM (Yoshida et al. 2003). While it is widely accepted that star-forming galaxies and accreting black holes were the primary sources of ionizing radiation for hydrogen reionization, there is still an ongoing debate regarding the relative contributions of these sources over time. However, the James Webb Space Telescope (JWST) along with other experiments featuring unique sensitivity, large wavelength coverage, and advanced spectroscopic and imaging capabilities may soon provide answers to these uncertainties (Finkelstein et al. 2015).

Ultraviolet radiation has the capability to ionize the hydrogen gas in the local vicinity of a radiation source, resulting in the creation of ionized bubbles within the gas. As these ionized bubbles merge, they encompass more radiation sources, leading to the accelerated expansion of ionization fronts that delineate their boundaries (Chen et al. 2023). This process triggers a chain reaction of bubble expansion until the mean free path of Lyman continuum (LyC) photons is controlled

by high-density regions referred to as Lyman Limit Systems (LLSs), which can retain a substantial fraction of their hydrogen in a neutral state. The mean free path of LyC can be determined from the absorption spectra of high-redshift quasars, and existing data point to a rapid decrease in the mean free path at redshift $z \sim 6$. However, observations suggest that this scenario is not fully realized in our universe. Whilst many simulations employ straightforward scaling relationships linking the total mass of Population III stars to the mass of the dark matter halo hosting them (Ghara et al. 2015), other potential sources of LyC radiation during reionization, such as dark matter annihilation (Mapelli et al. 2006; Liu et al. 2016), primordial globular clusters (dense clusters of stars formed in the early universe) (Ricotti 2002; Ma et al. 2022), and mini- or micro-quasars (Madau et al. 2004; Mirabel et al. 2011) are also under consideration (Gnedin & Madau 2022).

Studies involving quasar absorption spectra and Thomson scattering optical depth from CMB observations reveal that this transition occurs between $z \sim 6$ and 10 (Mitra et al. 2015). More precisely, the Planck Collaboration conducted recent observations on the temperature and polarization angular power spectra of the CMB. Their findings estimated τ to be 0.054 ± 0.007 , indicating that the midpoint of reionization occurred at $z \approx 7.7 \pm 0.6$ (Glazer et al. 2018). Nevertheless, some studies of quasars, such as Nasir & D’Aloisio (2020) imply that the end of the EoR may be at $z < 6$.

Notwithstanding, significant progress made in understanding cosmic reionization over the past decade (Datta et al. 2016), myriad questions remain unresolved regarding the underlying processes, geometry, and history of the EoR (Dayal & Ferrara 2018), and the Square Kilometre Array (SKA) will play a crucial role in unraveling these mysteries (Ali et al. 2015). Furthermore, researchers have utilized anisotropies in the CMB temperature map through the Sunyaev-Zel’dovich (SZ) effect to impose constraints on the EoR (Sunyaev & Zel’dovich 1980). Recent advancements in ground-based CMB observatories, such as the South Pole Telescope (SPT; Ruhl et al. 2004) and the Atacama Cosmology Telescope (ACT; Kosowsky 2003) have contributed to these efforts.

4. THE 21SSD SIMULATION

The 21SSD simulation dataset comprises the brightness temperature of 45 models that cover a selected 3D parameter space. These models were simulated at high and low resolutions, with a spatial resolution of 1024^3 elements, using the LICORICE code, which couples with hydrodynamics and computational execution simulation is $\sim 3 \times 10^6$ CPU hours (Baek et al. 2009). The 21SSD simulation considers heating and Wouthuysen-Field coupling by incorporating X-ray and Lyman line transfer processes into the model. In this simulation, the initial conditions for all models are the same,

and varying parameters are the Lyman band emissivity, f_α , the X-ray emissivity, f_X , and the hard-to-soft X-ray, $r_{H/S}$.

f_α : In §2, the correlation between the brightness temperature and the spin temperature was discussed. f_α is employed to quantify the efficiency of Lyman band emission. In accordance with Eq.6, the $Ly\alpha$ scattering coefficient, x_α , is identified as one of the parameters that remarkably influence the spin temperature. To calculate the local $Ly\alpha$ flux, radiative transfer calculations are conducted, disregarding the impacts of metal enrichment in the Lyman lines. A constant luminosity for the Lyman band is assumed, and the simulation calculates the energy emitted within a specific frequency range by a stellar population with different masses of stars is expressed as (Vonlanthen et al. 2011)

$$E(\nu_1, \nu_2) = \int_{\nu_1}^{\nu_2} \int_{M_{min}}^{M_{max}} \zeta(M)L(M, \nu)T_{life}(M)dM d\nu, \quad (8)$$

where $\zeta(M)$ represents the Initial Mass Function (IMF), $T_{life}(M)$ is the lifetime of a star with mass M , and $L(M, \nu)$ is the energy emission per time and frequency. Afterward, f_α is defined as the ratio of the energy effectively emitted in the simulation, E_{eff} , to the theoretical energy emission in the corresponding frequency range

$$f_\alpha = \frac{E_{eff}(\nu_\alpha, \nu_{limit})}{E(\nu_\alpha, \nu_{limit})}, \quad (9)$$

where ν_α and ν_{limit} are $Ly\alpha$ frequency and Lyman limit frequency. Increasing the value of f_α leads to enhanced prominence of peaks and troughs in the differential brightness temperature, but this change does not considerably impact the computational time required for the calculations. (Semelin et al. 2017). The determination of the brightness temperature in this research involves assigning the values of 0.5, 1, and 2 to f_α .

f_X : After recombination, T_k decreases steadily over time. However, X-ray heating eventually initiates a reversal in this trend, leading to a shift from the absorption to the emission regimes for the 21-cm signal. Due to the uncertainties surrounding the characteristics of high-redshift objects, it is not possible to accurately describe the high-redshift X-ray background with confidence. Therefore, it is reasonable to assume a correlation between the X-ray luminosity and the locally observed star formation rate (SFR). The effectiveness of X-ray generation during the EoR is typically characterized as (Furlanetto et al. 2006)

$$L_X = 3.4 \times 10^{40} f_X \left(\frac{SFR}{1M_\odot \cdot yr^{-1}} \right) erg \cdot s^{-1}. \quad (10)$$

An equivalent SFR is calculated for each newly generated source within the simulation by utilizing the source mass and lifetime. The X-ray luminosity of the source is then determined using a consistent f_X value throughout the entire simulation, employing the aforementioned formula. To account

for the uncertainty of the environment, f_X is considered as 0.1, 0.3, 1, 3, and 10.

$r_{H/S}$: X-ray heating sources mainly consist of binaries and active galactic nucleus (AGNs). X-ray heating from binaries results in more uniform heating that reduces 21-cm fluctuations during the heating transition. Hard X-rays have a high-energy and short-wavelength spectrum and receive special treatment in simulations due to their larger mean free path. On the other hand, soft X-rays from AGNs typically produce localized energy emissions and spatial variations. These soft X-rays have a spectral index of 1.6 and a range of energies between 0.1 and 2 keV (Fialkov et al. 2014; Furlanetto et al. 2006). f_X^{XRB} refers to the X-ray energy emitted by X-ray binaries, while f_X^{AGN} denotes the X-ray energy emitted by AGNs. Then, the fraction of hard X-ray emissions, $r_{H/S}$, is determined by the ratio of X-ray emissivities originating from X-ray binaries and AGNs

$$r_{H/S} = \frac{f_X^{XRB}}{f_X^{XRB} + f_X^{AGN}}. \quad (11)$$

In this study, $r_{H/S}$ is varied across the values of 0, 0.5, and 1. Moreover, we ensure uniformity in the initial conditions and the constants employed in the calculations across all simulations. The simulated environment for each model encompasses a spatial volume $200h^{-1} Mpc$ cube and contains 1024^3 particles, half of which are baryons, and the rest are dark matter.

The $Ly\alpha$ flux is estimated in a post-processing step by using a fixed grid with 512^3 cells which emit 4×10^8 photons once per 10^7 years. The simulation begins at $z = 100$ and uses second-order Lagrangian perturbation theory (2LPT) by the MUlti-Scale Initial Conditions package (Music code). The numerical integration of the system employs a dynamical timestep of 1 Myr, except for the case where the scale factor a is less than 0.03, a smaller timestep of 0.33 Myr is used. Additionally, the gravitational softening length applied in the simulation is $5ckpc$ (Semelin et al. 2017).

To preserve the compatibility of simulation results with observations, some astrophysical parameters have been fixed in the 21SSD simulation. For instance, within the LICORICE framework, the number of particles remains constant, and all baryonic particles possess uniform masses. Consequently, the process of star formation occurs exclusively within these baryonic particles. Once a particle exceeds a specific particular density, 100 times the mean baryonic density for the 21SSD simulation, it initiates star formation in accordance with the Kennicutt–Schmidt law where the exponent is set to one: $d\rho_s/dt = c_{eff}\rho_g$. Here, ρ_g is the gas density, ρ_s is the star density, and c_{eff} denotes an efficiency parameter (Bolgar 2018). In this case, c_{eff} can be interpreted as the reciprocal of the gas conversion time scale, which, in the simulations, is predetermined as $2Gyr$. Each star fraction emits

$\min(10^5, 5 \frac{10^7}{n_{bof\ sources}})$ packets of UV ionizing photons and an equal quantity of X-ray photons in each dynamical time step. IMF in the mass ranges $1.6M_\odot$ and $120M_\odot$ is used in MC sampling to determine the frequency of UV photons (Hahn & Abel 2011).

In this way, after the end of the simulation, $\sim 15 \times 10^9$ photon packets propagate. The fraction of ionizing UV photons escape for the unresolved structures is set to 0.2. The cosmological model utilized in the simulation is Λ CDM and constants are $H_0 = 67.8kms^{-1}$, $\Omega_m = 0.308$, $\Omega_\Lambda = 0.692$, $\Omega_b = 0.0484$, $\sigma_8 = 0.8149$, $n_s = 0.968$, and $\tau = 0.0692$ (Planck collaboration et al. 2014; Semelin et al. 2017).

For each model, the resulting dataset consists of 135 brightness temperature lightcones, generated in the x, y, or z direction, at high and SKA resolutions ranging from approximately $\Delta\theta \sim 0.3'$ to $3' - 8'$ respectively. This dataset offers enhanced resolution and improved physical accuracy in comparison to similar databases, like the one presented by Mesinger et al. (2016). The 21cmFAST simulation encompasses a significantly greater cosmological expanse while maintaining an equal number of resolution elements, resulting in reduced spatial resolution.

5. METHODS

ML methods have enabled cosmologists to analyze data more effectively in recent years. These methods involve creating and applying algorithms that discover patterns in data Ntampaka et al. (2019). ML algorithms can identify patterns in high-dimensional spaces. Thus, simulations can act as a laboratory for finding patterns that are not obvious and enhancing our comprehension of the physics governing the phenomena being studied (Dvorkin et al. 2022).

5.1. Multilayer Perceptron

Neural networks are artificial systems that mimic the biological brain and the nervous system (Sazli 2006). They learn abstract features by using activation functions that apply non-linear transformations (Kim 2021). A neuron is a basic unit of neural networks that can process information. As a matter of fact, it receives weighted information from other neurons through synaptic connections and generates an output by applying an activation function to the weighted sum of those input signals (Sazli 2006). The \tanh function is an activation function that has been used in neural networks and has the zero-centric property (Dubey et al. 2022).

A feedforward neural network, or an MLP algorithm, usually consists of several fully connected layers that have non-linear activation functions (Kim 2021). MLPs can approximate continuous non-linear functions universally and can learn from input-output patterns. They also have complex network architectures with multiple inputs and outputs (Smola & Schölkopf 2004). The hidden layer is a group of

neurons that uses an activation function and acts as an intermediate layer between the input layer and the output layer (Karsoliya 2012). The neuron outputs from the hidden layer are derived through computation as follows (Popescu et al. 2009)

$$y_j(p) = f\left(\sum_{i=1}^n x_i(p) \cdot \omega_{ij} - \theta_j\right), \quad (12)$$

where y_j represents the output of neuron j , f is the sigmoid activation function, n is the number of inputs for a particular neuron j in the hidden layer, x_i is the input value of the i -th neuron in the previous layer, ω_{ij} is the weight associated with each input (for each neuron), and θ_j is the bias term for neuron j . The final output of the network is (Popescu et al. 2009)

$$y_k(p) = f\left(\sum_{i=1}^m x_{jk}(p) \cdot \omega_{jk} - \theta_k\right), \quad (13)$$

where m is the number of inputs for the neuron k from the output layer. We use Adam (Kingma & Ba 2014), a solver for weight optimization, which is a gradient-based optimization algorithm for stochastic objective functions, based on adaptive estimates of lower-order moments. The method is easy to implement, fast, memory-efficient, invariant to diagonal rescaling of the gradients, and suitable for large problems in terms of data and parameters. The method also works well for non-stationary objectives and problems with very noisy and sparse gradients.

The hyperparameters (HP) are easy to understand and usually need little tuning. We update the initial parameter vector where our parameter vector at the given step does not converge (Kingma & Ba 2014)

$$\omega_t \leftarrow \omega_{t-1} - \alpha \cdot \hat{m}_t / (\sqrt{\hat{v}_t} + \epsilon), \quad (14)$$

where $\alpha = 0.0001$ is stepsize which defines the learning rate, \hat{m}_t and \hat{v}_t are the first and second order moments of gradient, and ϵ is a small constant (usually 10^{-7}) used to avoid division by zero.

5.2. Support Vector Regression

Recently, Support Vector Machines (SVM) have emerged from the framework of statistical learning theory (Wang 2005). Unlike neural networks, SVM does not suffer from local optima, and the training is fairly easy. It also performs well on high dimensional data, and it has explicit control over the trade-off between classifier complexity and error (Smola & Schölkopf 2004). The principle of maximal margin, dual theory, and kernel trick are the three core elements that make SVMs successful (Tian et al. 2012). In the maximum margin method, the solution only depends on the support vectors, and the supporting planes are pushed apart until they bump into the support vectors (Bennett & Campbell 2000). The

standard SVM is a maximum margin classifier that has a hyperplane as its decision function, which maximally separates samples from different classes. The formulation of the SVM is based on this principle (Salcedo-Sanz et al. 2014).

SVR is a technique that uses kernels to estimate a function from an infinite-dimensional function space, based on a finite number of observations at specific points. This is a generalization of the classification problem (Salzo & Suykens 2020). Given that $x_i \in \mathbb{R}^n$ is a feature vector and $z_i \in \mathbb{R}^1$ is the corresponding output, $(x_1, z_1), \dots, (x_l, z_l)$ is the set of training points. The standard SVR is

$$\min_{\omega, b, \xi, \xi^*} \frac{1}{2} \omega^T \omega + C \sum_{i=1}^l \xi_i + C \sum_{i=1}^l \xi_i^*, \quad (15)$$

with the following restrictions

$$\begin{cases} \omega^T \phi(x_i) + b - y_i \leq \epsilon + \xi_i \\ y_i - \omega^T \phi(x_i) - b \leq \epsilon + \xi_i^* \\ \xi_i, \xi_i^* \geq 0 \quad i = 1, \dots, l \end{cases},$$

where b is the scalar bias term, ξ_i and ξ_i^* are slack variables to determine the deviation of training, and C is the regularization hyperparameter that determines the trade-off between minimizing the error and maximizing the margin. $\epsilon > 0$ is a hyperparameter that determines the width of the ϵ -insensitive tube and $\phi(x_i)$ maps x_i into a higher-dimensional space (Chang & Lin 2011). Indeed, C has a crucial role in balancing the smoothness against the allowance for deviations beyond a certain threshold ϵ . This is achieved by utilizing a loss function known as $|\xi|_\epsilon$ -insensitive, which is defined by (Smola & Schölkopf 2004)

$$|\xi|_\epsilon := \begin{cases} 0 & \text{if } |\xi| \leq \epsilon \\ |\xi| - \epsilon & \text{otherwise} \end{cases}. \quad (16)$$

Due to the possible high dimensionality of the vector variable ω , usually we solve the following dual problem (Chang & Lin 2011).

To utilize SVM for training, it is necessary to address a quadratic programming problem, also known as a quadratic optimization problem. SVM offers the primal formulation and the dual formulation for this. The dual optimization problem is expressed in terms of Lagrange multipliers and the bias (Dias & Neto 2016). Solving the primal problem directly proves challenging due to the complexity of its constraints. However, by applying the mathematical technique of Lagrangian duality theory, the problem can be simplified (Bottou et al. 2007). This approach allows for solving the corresponding dual problem, which offers several advantages. Firstly, even when the primal problem is not convex, the dual problem will still have a unique optimal solution. Secondly, the optimal function value of the primal form has

a lower bound, which is the objective function value. Finally, solving the optimization problem in the dual form can be done more quickly and effectively, as it may have fewer variables compared to the primal form (Awad & Khanna 2015). The dual problem is

$$\min_{\alpha, \alpha^*} \frac{1}{2}(\alpha - \alpha^*)^T Q(\alpha - \alpha^*) + \epsilon \sum_{i=1}^l (\alpha_i + \alpha_i^*) + \sum_{i=1}^l y_i(\alpha_i - \alpha_i^*), \quad (17)$$

satisfying the following requirements

$$\begin{cases} e^T(\alpha - \alpha^*) = 0 \\ 0 \leq \alpha_i, \alpha_i^* \leq C \quad i = 1, \dots, l \end{cases},$$

where α_i and α_i^* are vectors of Lagrange multipliers associated with the training samples and support vectors. e^T is the transpose of a vector e , which is a vector of ones and $Q_{ij} = K(x_i, x_j) \equiv \phi(x_i)^T \phi(x_j)$ is the kernel function. Consequently, the prediction is

$$y_i = \sum_{i \in SV} (\alpha - \alpha^*)K(x_i, x) + b, \quad (18)$$

where $(\alpha_i - \alpha_i^*)$ are dual coefficients, n is the number of training examples, x is the input to be predicted, and x_i is the i -th training example.

A kernel function can be any function that complies with Mercer's theorem (Wang et al. 2003). In fact, the kernel is used to build a model in a feature space with higher dimensions, without needing to specify the mapping function from the input space to the feature space. This way, the input space can be linearly separable in the feature space for non-linear separable cases. Furthermore, the hyperplane can efficiently serve as a decision boundary in this setting (Rohmah et al. 2021).

The radial basis functions (RBFs) approximation is a powerful technique that provides accurate results without relying on a mesh. In the RBFs method, each function denoted as $\phi(r) = \exp(-(\epsilon r)^2)$, depends solely on the distance $|r|$ between a center point and the corresponding field point or source, with a shape parameter, ϵ , involved (Karimi et al. 2020). An isotropic stationary kernel, known as the RBF kernel, is defined by a function $\psi : [0, \infty) \rightarrow \mathbb{R}$, satisfying the equation (Zhang et al. 2004)

$$K(x, y) = \psi(-\|x - y\|). \quad (19)$$

The Gaussian kernel is commonly used in the RBF case, with the spread parameter σ playing a crucial role in the generalization performance of SVMs (Wang et al. 2003).

$$K(x, y) = \exp(-\|x - y\|^2 / (2\sigma^2)) \quad (20)$$

5.3. Grid search

HPs can be highly configured for ML algorithms. Grid search (GS) is the technique of splitting the range of each HP into discrete values and trying every combination of values. Numeric and integer HP values are usually uniformly spaced in their box constraints. The number of distinct values per HP is the resolution of the grid. For categorical HPs, either a subset or all possible values are chosen (Bischl et al. 2023).

5.4. The Architecture Behind this Work

In this paper, we conducted all of our research on a simulated global 21-cm signal. The dataset consisted of 18,000 simulated data of global 21-cm signals with different astrophysical parameters in the EoR, with a test size of 10% and a train size of 90%. For SVR method, we have used the following hyperparameters: $C=100$, $\gamma = 1/2\sigma^2=25$, and $\epsilon=0.001$. As for the MLP, we have employed a hidden layer structure of (100, 50, 100, 50, 100). These choices were made to ensure appropriate training and evaluation of the models in our study.

SVR requires fewer hyperparameters (kernel function, regularization parameter, and epsilon) compared to MLP (number of layers, nodes, activation function, learning rate, momentum, regularization). SVR tends to converge to a global optimum since it is a convex optimization problem, while MLP can have multiple local optima. The stochastic nature of MLP introduces prediction variability due to random initialization and data shuffling, making SVR more reliable (Kingma & Ba 2014). Therefore, despite the optimization of each algorithm for optimal results, we expect that the SVR algorithm will demonstrate more robust outcomes. Moreover, we practically need to observe the superiority of MLP and SVR in the results of this work. One common approach is calculating the coefficient of determination, often represented as R^2 -score, R^2 .

This coefficient measures how well the independent variables in a model explain the variability of the dependent variable by

$$R^2(y, \hat{y}) = 1 - \frac{\sum_{i=1}^n (y_i - \hat{y}_i)^2}{\sum_{i=1}^n (y_i - \bar{y})^2}, \quad (21)$$

where y is the observed data, \bar{y} represents the average of observed data, and \hat{y} is the predicted data by the algorithm (Chicco et al. 2021). The coefficient of determination ranges between $(-\infty, 1]$ with 1.0 indicating perfect predictions, reflecting the relationship between the ground truth and the prediction model. One could argue that in order to guarantee the robustness of the results, the validation dataset must be distinct from the training dataset. However, it is worth mentioning that the issue of reconstruction error typically emerges from changes in dimensionality. To address this concern, we have accounted for it by calculating the R^2 -score during the computations (Tripathi et al. 2024).

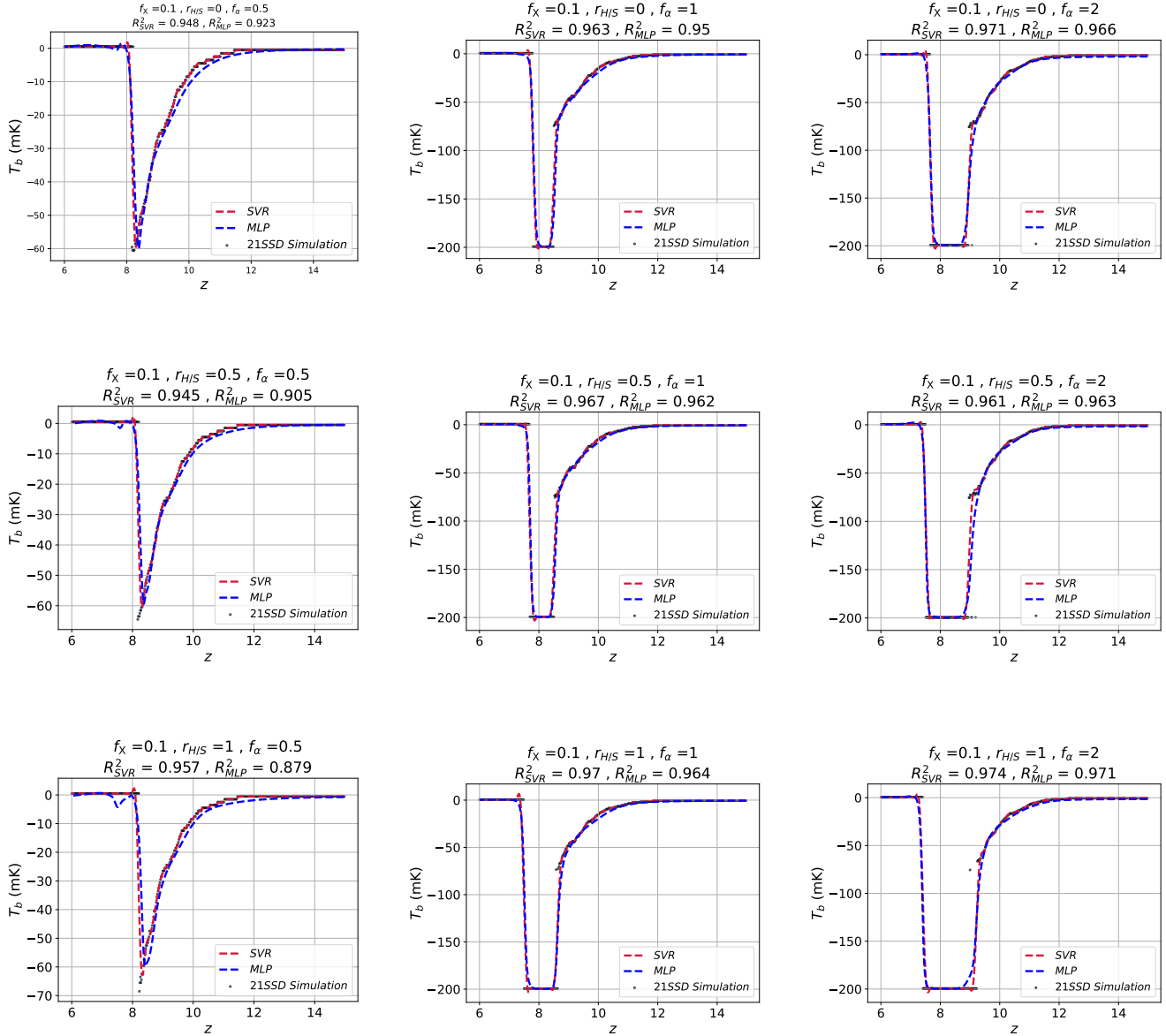


Figure 1. These plots compare MLP and SVR algorithms in characterizing the IGM for $f_X = 0.1$. The dots show the results of the 21SSD simulation and the blue and red dash lines show MLP and SVR outputs, respectively. Both algorithms capture trends and approximate the minimum point. However, MLP struggles with accurate estimation of high redshift points when $f_\alpha = 0.5$, leading to inconsistencies and reduced reliability. In contrast, SVR performs better for $z > 8$, with a small peak observed in the range $7 < z < 8$. These differences are reflected in the R^2 coefficient, highlighting the varying performance of the algorithms.

6. RESULT

Given that the 21SSD simulation requires powerful hardware resources due to its computational intensity, our main goal is to utilize ML techniques to obtain the results from the IGM simulations swiftly without sacrificing precision. We aim to obtain brightness temperature data within significantly reduced timeframes by adjusting the free parameters, f_α , f_X , and r_{HIS} . To achieve this, we employ the MLP and SVR algorithms. In §5, we introduced and elucidated both of these

algorithms. Furthermore, in §5.4, we provided detailed explanations of their implementation under specific values and conditions within this study. The results obtained from our experiments can be observed in Figures 1 to 5, which serve as visual representations of the obtained outputs.

Under the condition of $f_X = 0.1$, both the MLP and SVR algorithms successfully capture the general trends and approximate the minimum point on the graph. However, challenges arise when attempting to accurately estimate the high

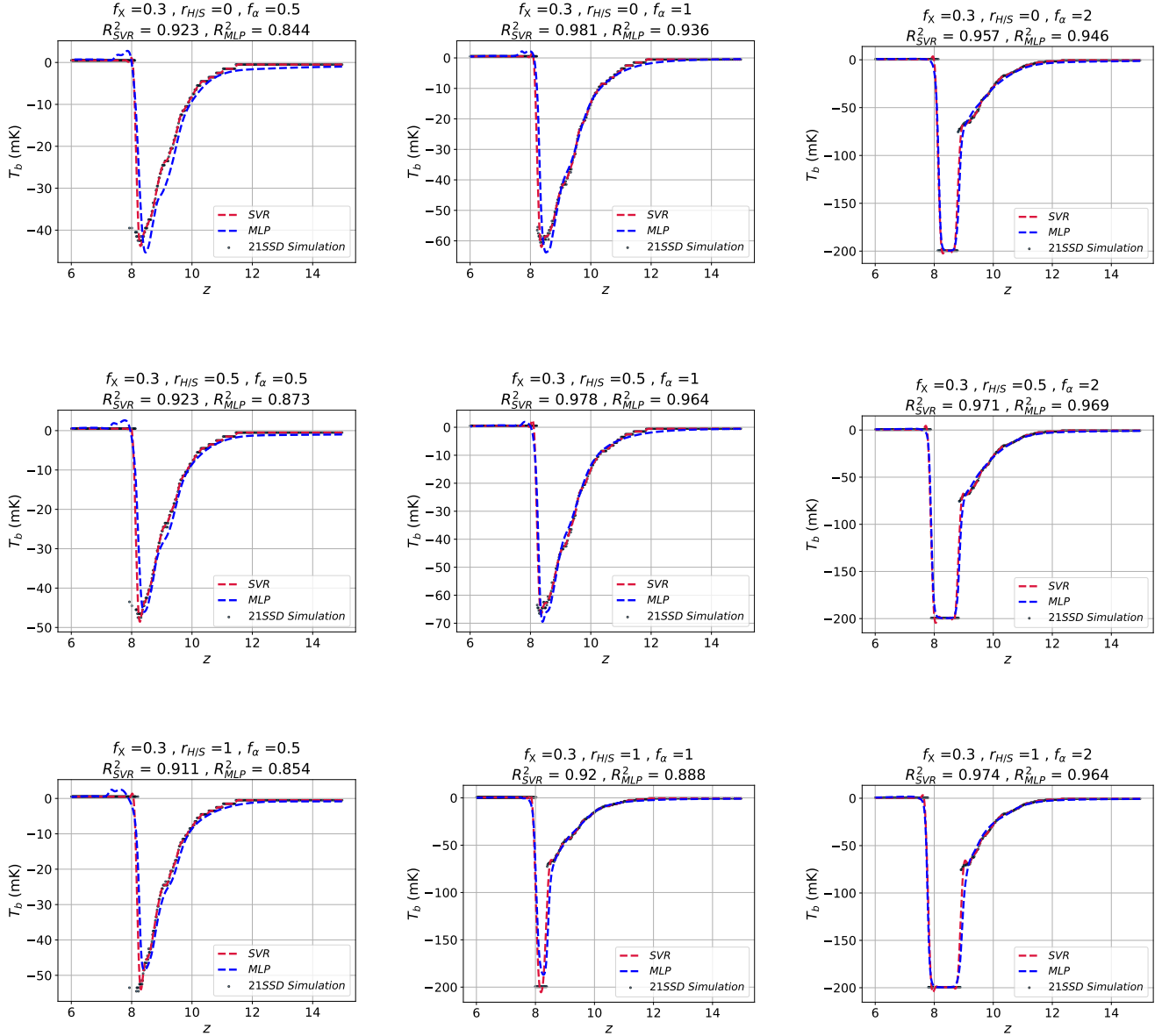


Figure 2. In this figure, the IGM analysis for $f_X = 0.3$ is investigated. The dots show the results of the 21SSD simulation and the blue and red dash lines show MLP and SVR outputs, respectively. Inconsistencies persist for MLP when $f_X = 0.3$ and $f_\alpha = 0.5$, even extending to $f_\alpha = 1$. The SVR algorithm shows improved performance with a reduced peak at $z \sim 8$, while MLP exhibits increased fluctuations in the same range for $f_\alpha = 0.5$. MLP fails to reach the minimum point for $f_\alpha = 0.5, 1$, and $r_{HIS} = 1$, with the ascending process starting at a higher redshift. However, for $r_{HIS} = 0$, MLP achieves a deeper descent. The MLP algorithm also experiences increased deviations, especially at the minimum point, and redshifts between 7 and 8. In contrast, the SVR algorithm performs exceptionally well with minimal inaccuracy.

redshift points in the case of $f_\alpha = 0.5$ for MLP. The discrepancy, particularly prominent in Fig.1 when f_α is set to 0.5, erodes the reliability and precision of the MLP algorithm for accurate analytical purposes. The SVR algorithm exhibits superior performance for $z > 8$, despite manifesting a small peak within the range $7 < z < 8$. These divergences are also reflected in the R^2 -score.

In the case of $f_X = 0.3$ and $f_\alpha = 0.5$, inconsistencies persist and even extend to $f_\alpha = 1$ for the MLP algorithm. The peak observed at $z \sim 8$ for the SVR algorithm has improved, while for MLP, the range of fluctuations has increased for $f_\alpha = 0.5$. Fig.2 shows that the MLP algorithm does not reach the minimum points for $f_\alpha = 0.5$ and 1 with $r_{HIS} = 1$, and the ascending process starts at a higher redshift, however, for $r_{HIS} = 0$, it goes deeper. By examining the values of R^2 , it

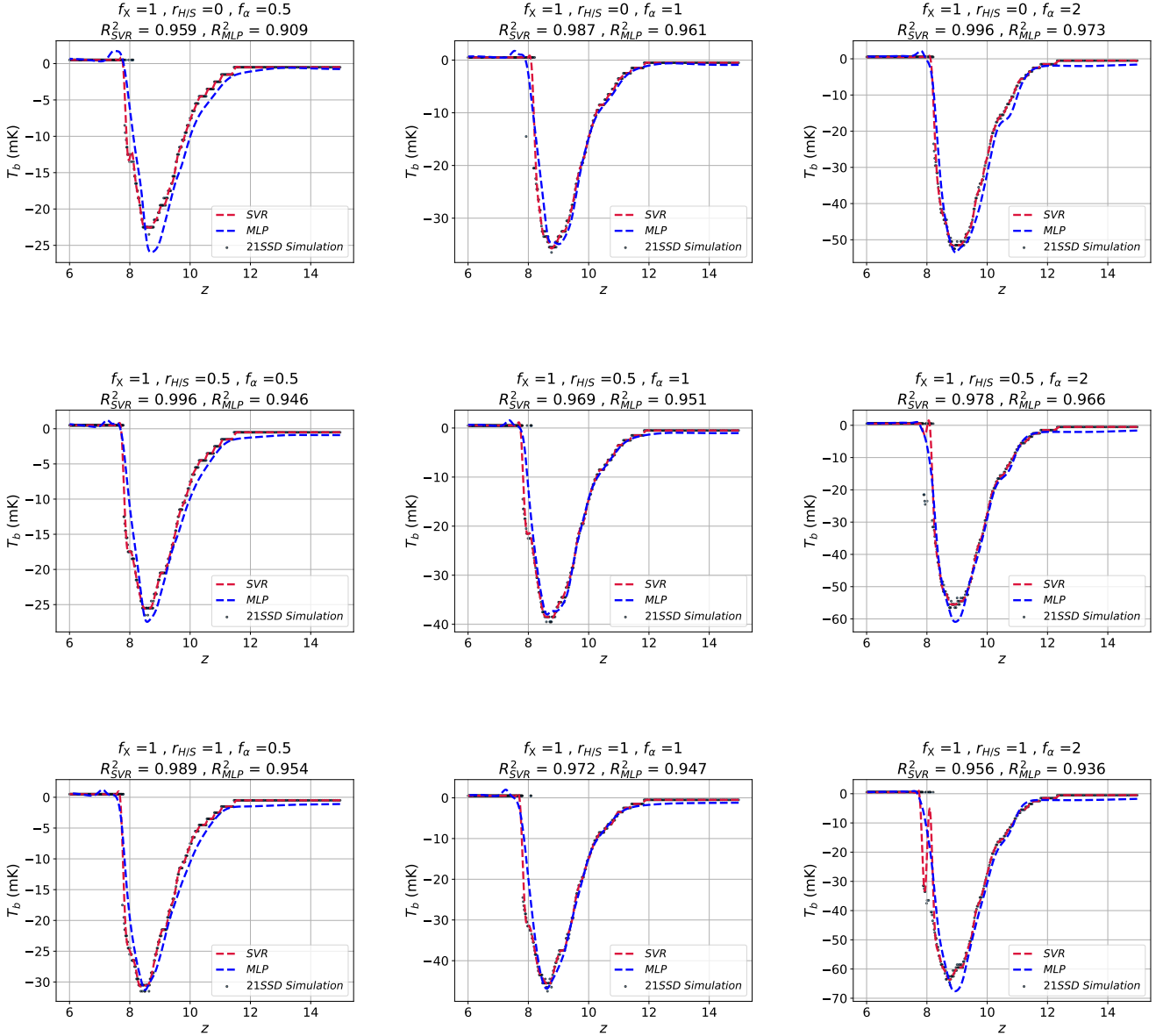


Figure 3. The IGM characterization for $f_X = 1$ can be seen in these plots. The dots show the results of the 21SSD simulation and the blue and red dash lines show MLP and SVR outputs, respectively. SVR shows precise data reconstruction, achieving an impressive minimum R^2 value of 0.956, with the highest performance reaching 0.996. In contrast, MLP struggles to accurately capture the data, exhibiting larger discrepancies and difficulties in determining depth and reaching $T_b = 0$ for different conditions. SVR demonstrates superior performance over MLP in this condition.

can be determined that the deviations for the MLP algorithm, especially at the minimum point and redshifts between 7 and 8, have increased. In contrast, the SVR algorithm performs exceptionally well without notable inexactness.

At $f_X = 1$, SVR accurately reconstructs the data, achieving a minimum R^2 value of 0.956, indicating the potential for further improvement through better coefficient adjustments and mitigating the existing overfitting issue observed at $z \sim 8$. Under these conditions, the best R^2 -score obtained for SVR

is 0.996. Fig.3 clearly demonstrates the superiority of SVR over MLP. Specifically, for $f_\alpha = 1$, despite correctly capturing the overall trend, the MLP algorithm exhibits a larger discrepancy between the points compared to the results of the 21SSD simulation. It encounters difficulties in accurately determining the minimum points and also experiences delays in reaching $T_b = 0$ in certain instances.

Considering $f_X = 3$ in Fig.4, similar to the previously examined scenarios for MLP, $f_\alpha = 0.5$ yields the weakest out-

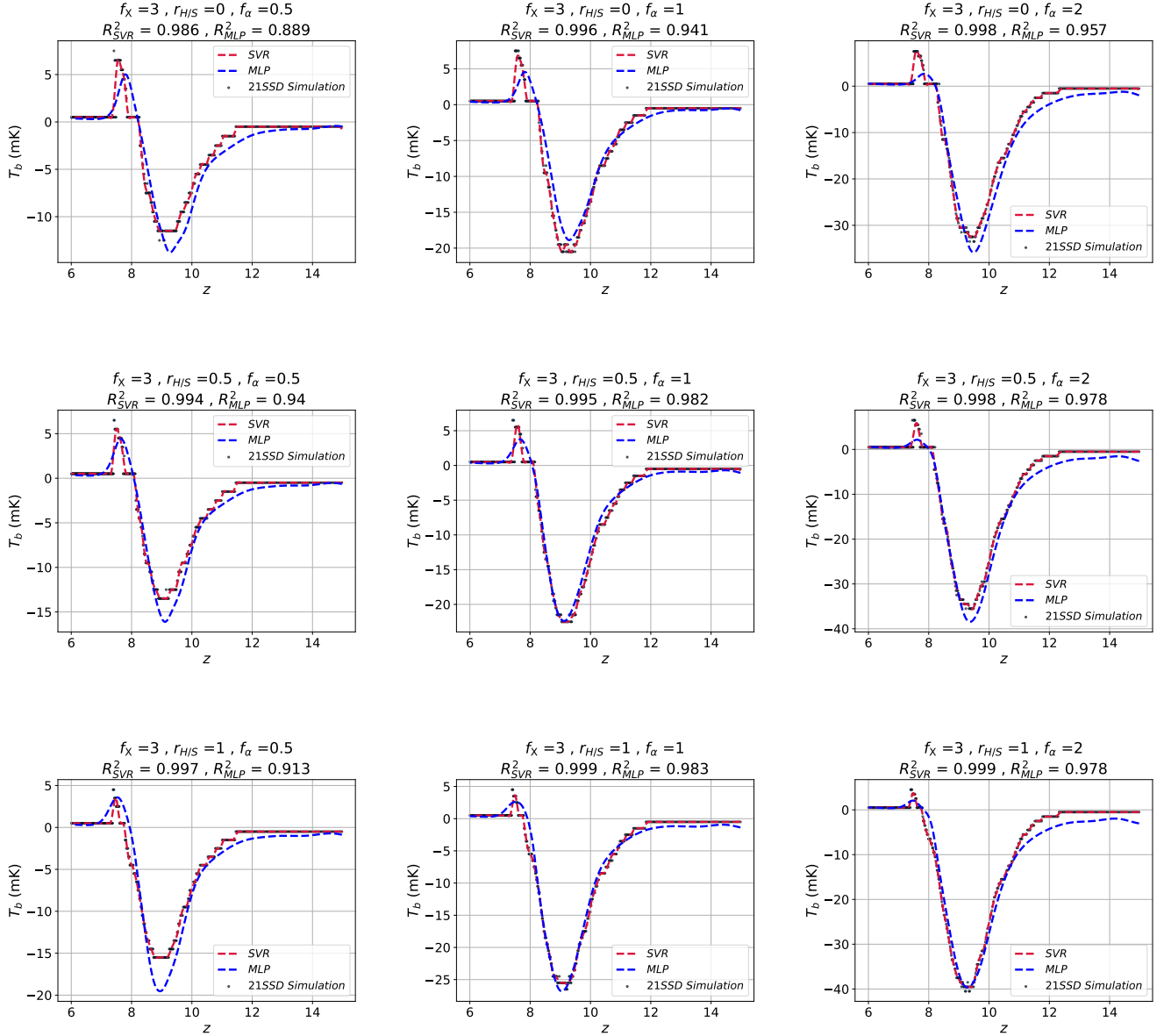


Figure 4. The results of ML algorithms with 21SSD simulation for $f_X = 3$ are shown in this figure. The dots show the results of the 21SSD simulation and the blue and red dash lines show MLP and SVR outputs, respectively. MLP struggles with the condition $f_\alpha = 0.5$, resulting in a weaker output with an R^2 coefficient of 0.889. Additionally, MLP encounters difficulties in accurately identifying the minimum temperature value and also fails to follow the observed peak in the range $7 < z < 8$. In contrast, the SVR algorithm accurately tracks even the smallest changes, particularly at high redshifts.

put compared to other conditions with $R^2=0.889$. For $f_\alpha > 1$, deviations can be observed in the brightness temperature at higher redshifts, and MLP only reaches the temperature of the IGM at $r_{HIS} = 0$ and $f_\alpha = 0.5$. It encounters difficulties in accurately identifying the location and value of the minimum temperature, and it does not follow the peak observed at $7 < z < 8$. On the other hand, the SVR algorithm performs accurately in tracking even the smallest changes, particularly at redshifts greater than 10.

In high X-ray environments, $f_X = 10$, regardless of the value of f_α , the MLP algorithm predictions for the brightness temperature become unreliable. Even at $r_{HIS} = 1$ and $f_\alpha = 0.5$, the R^2 -score reaches 0.659, indicating significantly poorer performance compared to SVR. In environments characterized by significant temperature fluctuations, the SVR algorithm exhibits exceptional precision by effectively matching its predictions with the data obtained from the 21SSD simulation. As depicted in Fig.5, the lowest achieved R^2 co-

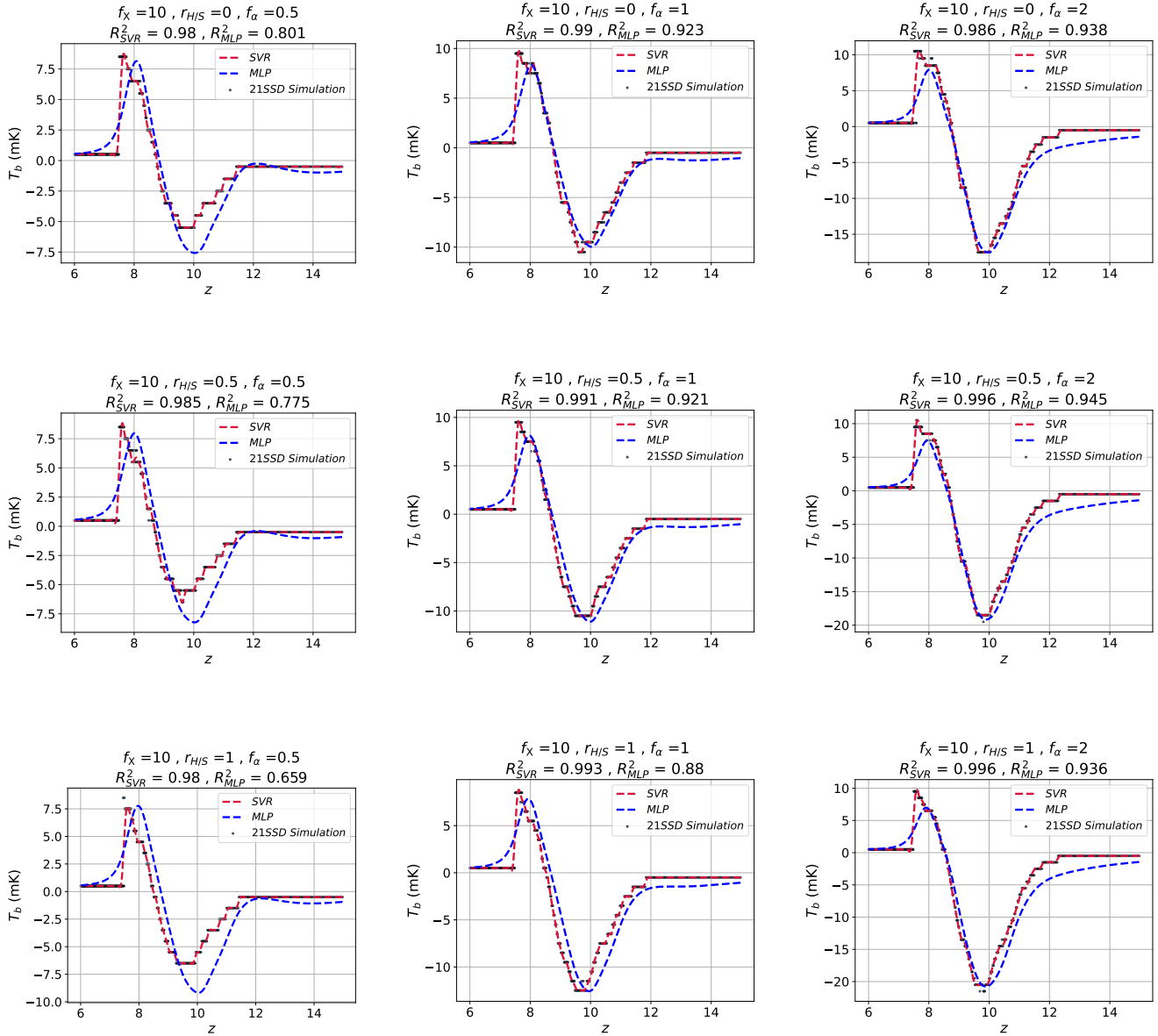


Figure 5. These plots present ML algorithms in characterizing the IGM for $f_X = 10$. The dots show the results of the 21SSD simulation and the blue and red dash lines show MLP and SVR outputs, respectively. with $f_X = 10$, the MLP algorithm performs poorly in predicting brightness temperature, regardless of f_α . Even at $r_{HIS} = 1$ and $f_\alpha = 0.5$, MLP achieves a low R^2 -score of 0.659. In contrast, SVR demonstrates remarkable accuracy, aligning its predictions with the 21SSD simulation data. The lowest achieved R^2 coefficient for SVR is 0.98. MLP struggles with temperature fluctuations and depth-related issues, making it unreliable.

efficient for SVR is 0.98. In contrast, the MLP algorithm deviates significantly from the 21SSD data for redshifts over 9 and continues to struggle with the depth issue. The main challenge for MLP lies in its inability to match the temperature fluctuations present in the main dataset. Consequently, it is not reliable to rely on the MLP output in this regard. For instance, if the parameter of interest is the neutral hydrogen fraction, given the temporal significance in this study, rely-

ing on the MLP algorithm may not be a suitable method for reconstruction.

The outputs generated by the SVR algorithm effectively characterize the IGM and display a high level of dependability. However, to reduce the risk of overfitting, the careful selection of training data becomes critically important. It is crucial to realize that the brightness temperature inherently includes fluctuations that should not be eliminated during the ML process.

It becomes evident that SVR is a suitable algorithm for efficiently describing the IGM. The reliability of the data used for both SVR and the comparative algorithms is ensured by sourcing it from simulation 21SSD, as discussed in §4. Moreover, considering the utilization of 18,000 data points in the respective training of MLP, where 10% of the data was used for testing and 90% for learning, the overall R^2 -score for MLP is 0.957, while for SVR it is 0.972. This indicates that SVR has performed better overall in terms of R^2 .

Apart from the better accuracy of SVR, considering the computational times for MLP and SVR which are 0.0962 and 3.4886 CPU hours, respectively, it is more time-efficient to utilize these machine learning algorithms instead of running the 21SSD simulation with new coefficients.

7. CONCLUSION

The EoR holds meaningful importance not only for studying the behavior of the neutral hydrogen fraction, but also for understanding the role of dark matter in the evolution of the universe. Baryons, including neutral hydrogens, act as tracers of the underlying dark matter distribution. Therefore, studying the neutral hydrogen fraction during the EoR provides valuable insights into the interplay between dark matter and baryonic matter. By investigating the ionization state of the IGM and the impact of ionizing photons on neutral hydrogens, researchers can further unravel the intricate relationship between dark matter, baryons, and the EoR.

To comprehend the EoR, sophisticated simulations have been employed, and the 21SSD simulation emerging as one of the foremost options. The 21SSD simulation focuses specifically on the EoR and offers advantages, such as the consideration of essential parameters (f_X , f_α , and $r_{H/S}$) and the generation of brightness temperature in informative plots at different redshifts. Moreover, another aspect of the 21SSD simulation is the findings are readily available to the public.

To overcome the challenges posed by the complexity, duration, and resource requirements of previous simulations of the IGM, this study explores ML techniques. By training ML models on existing simulation data, these models can learn the underlying trends and relationships within the IGM. Specifically, the MLP and SVR algorithms are employed as alternative methods to alleviate the computational burden. By leveraging the datasets produced by the 21SSD simulation, the SVR algorithm showcases exceptional precision in predicting brightness temperature changes concerning redshift for different free parameter values.

MLP demonstrates good performance for $z < 7$ and $z > 10$ in capturing the general trends of the IGM at $f_X = 0.1$, although it struggles to estimate the minimum values accurately in $r_{H/S} = 1$ and $f_\alpha = 0.5$. However, the discrepancies between the MLP predictions and the 21SSD simulation, particularly around redshift 7, undermine its reliability for accu-

rate analysis. In contrast, the SVR algorithm consistently exhibits impressive precision in capturing the low points, subsequent increases, and minor fluctuations, as demonstrated in Fig.1.

The challenges for the MLP algorithm persist when examining $f_X = 0.3$, particularly in estimating the extremums for redshifts below 10. The discrepancies become more pronounced when considering $f_\alpha = 0.5$, affecting the reliability and accuracy of MLP. On the other hand, the SVR algorithm continues to perform exceptionally well, accurately tracking the data points and maintaining consistency with the 21SSD simulation, apart from a minor discrepancy at a redshift of approximately 8 for specific parameter combinations.

At higher X-ray fractions, such as $f_X = 1$, the MLP performance diminishes, especially for redshifts above 9, showing deviations from the expected trend. In contrast, the SVR reliability and precision are further highlighted by achieving a minimum R^2 value of 0.956 as shown in Fig.3.

When considering $f_X = 3$, MLP faces challenges in accurately determining the minimum temperature and tracking the peak in the temperature at $7 < z < 8$, especially for $f_\alpha > 1$. It shows a weaker performance, achieving an R^2 value of 0.889 for $f_\alpha = 0.5$. On the other hand, the SVR algorithm consistently captures even subtle variations, particularly at redshifts greater than 10, showcasing its precision and dependability.

In $f_X = 10$, regardless of the value of f_α , the predictions of the MLP algorithm for the brightness temperature remain unreliable. MLP struggles to match the temperature fluctuations present in the main dataset, deviating significantly from the 21SSD data for redshifts over 9. Conversely, the SVR algorithm illustrates remarkable accuracy, achieving a minimum R^2 value of 0.98 and effectively aligning its predictions with the data from the 21SSD simulation.

Utilizing ML techniques, such as SVR, within the IGM simulations, including the 21SSD simulation, holds great potential for advancing our understanding of the evolutionary patterns of various cosmological and astrophysical parameters during the EoR. These approaches enable researchers to explore the interplay of various parameters and obtain accurate predictions with reduced computational requirements. The temporal demands for the 21SSD simulation amount to approximately 3×10^6 CPU hours, whereas the MLP algorithm necessitates a mere 0.0962 CPU hours, and the SVR algorithm requires 3.4886 CPU hours. As a result, both the MLP and SVR algorithms present a substantial acceleration in computational efficiency compared to the 21SSD simulation, with MLP exhibiting a speed improvement of roughly 10^6 times, and SVR demonstrating an even more impressive advancement of approximately 10^7 times.

The efficacy of SVR as a valuable tool in overcoming the computational challenges of complex simulations is evident.

In this study, SVR has been employed to examine the brightness temperature. However, in a broader context, leveraging training data from extensive simulations, such as N-body simulations, that capture the evolution of parameters can enable the algorithm to be applied to a delimited number of samples and estimate other states. Furthermore, it enables the prediction of other parameters of the IGM and even different physical phenomena. Future endeavors have the opportunity to delve deeper into the application of ML algorithms in cosmology and astrophysics, leveraging their potential to save time and resources. This holds great potential for further advancements in our knowledge of the universe.

Several related studies, including [Bye et al. \(2022\)](#), [Bevins et al. \(2021\)](#), and [Breitman et al. \(2024\)](#), have introduced various emulators based on neural network algorithms. Theoretically, neural networks have inherent stochastic behavior and

can be designed with different architectures, involving varying arrangements of neuron layers. The choice of activation functions also plays a crucial role in determining the activation of specific neurons, thereby significantly influencing the performance of neural networks. However, this work demonstrates that SVR with its kernel trick produces more accurate results. Moreover, we put our theoretical expectations into practice and found that SVR outperforms MLP, especially in complex environments, producing more accurate results. Consequently, it becomes necessary to transition from neural network-based algorithms to SVR in order to obtain improved accuracy in emulations. Furthermore, the LoReLi database, which encompasses a significant volume of simulations ([Meriot & Semelin 2023](#)), shows great potential as a valuable resource for the development of an emulator using SVR in future research endeavors.

REFERENCES

- Ali, Z. S., Parsons, A. R., Zheng, H., et al. 2015, *The Astrophysical Journal*, 809, 61
- Awad, M., & Khanna, R. 2015, *Efficient learning machines: theories, concepts, and applications for engineers and system designers* (Springer nature)
- Baek, S., Di Matteo, P., Semelin, B., Combes, F., & Revaz, Y. 2009, *Astronomy & Astrophysics*, 495, 389
- Barkana, R., & Loeb, A. 2001, *Physics reports*, 349, 125
- Bennett, K. P., & Campbell, C. 2000, *ACM SIGKDD explorations newsletter*, 2, 1
- Bevins, H., Handley, W., Fialkov, A., de Lera Acedo, E., & Javid, K. 2021, *Monthly Notices of the Royal Astronomical Society*, 508, 2923
- Bischl, B., Binder, M., Lang, M., et al. 2023, *Wiley Interdisciplinary Reviews: Data Mining and Knowledge Discovery*, 13, e1484
- Bolgar, F. 2018, PhD thesis, Sorbonne université
- Bottou, L., Lin, C.-J., et al. 2007, *Large scale kernel machines*, 3, 301
- Bowman, J. D., Rogers, A. E., Monsalve, R. A., Mozdzen, T. J., & Mahesh, N. 2018, *Nature*, 555, 67
- Breitman, D., Mesinger, A., Murray, S. G., et al. 2024, *Monthly Notices of the Royal Astronomical Society*, 527, 9833
- Bye, C. H., Portillo, S. K., & Fialkov, A. 2022, *The Astrophysical Journal*, 930, 79
- Chang, C.-C., & Lin, C.-J. 2011, *ACM transactions on intelligent systems and technology (TIST)*, 2, 1
- Chardin, J., Uhlrich, G., Aubert, D., et al. 2019, *Monthly Notices of the Royal Astronomical Society*, 490, 1055
- Chen, H.-W., Prochaska, J. X., & Gnedin, N. Y. 2007, *The Astrophysical Journal*, 667, L125
- Chen, N., Trac, H., Mukherjee, S., & Cen, R. 2023, *The Astrophysical Journal*, 943, 138
- Chicco, D., Warrens, M. J., & Jurman, G. 2021, *PeerJ Computer Science*, 7, e623
- Datta, K. K., Ghara, R., Majumdar, S., et al. 2016, *Journal of Astrophysics and Astronomy*, 37, 1
- Dayal, P., & Ferrara, A. 2018, *Physics Reports*, 780, 1
- Dias, M. L. D., & Neto, A. R. R. 2016, in *2016 IEEE congress on evolutionary computation (CEC)*, IEEE, 2185–2192
- Dillon, J. S., Liu, A., Williams, C. L., et al. 2014, *Physical Review D*, 89, 023002
- Dubey, S. R., Singh, S. K., & Chaudhuri, B. B. 2022, *Neurocomputing*
- Dvorkin, C., Mishra-Sharma, S., Nord, B., et al. 2022, *arXiv preprint arXiv:2203.08056*
- Ewen, H. I., & Purcell, E. M. 1951, *Nature*, 168, 356
- Fan, X., Strauss, M. A., Becker, R. H., et al. 2006, *The Astronomical Journal*, 132, 117
- Fialkov, A., Barkana, R., & Visbal, E. 2014, *Nature*, 506, 197
- Field, G. B. 1958, *Proceedings of the IRE*, 46, 240
- . 1959, *Astrophysical Journal*, vol. 129, p. 525, 129, 525
- Finkelstein, S. L., Ryan, R. E., Papovich, C., et al. 2015, *The Astrophysical Journal*, 810, 71
- Furlanetto, S. R., Oh, S. P., & Briggs, F. H. 2006, *Physics reports*, 433, 181
- Ghara, R., Choudhury, T. R., & Datta, K. K. 2015, *Monthly Notices of the Royal Astronomical Society*, 447, 1806
- Glazer, D., Rau, M. M., & Trac, H. 2018, *arXiv preprint arXiv:1808.00553*
- Gnedin, N. Y., & Madau, P. 2022, *Living Reviews in Computational Astrophysics*, 8, 3

- Hahn, O., & Abel, T. 2011, *Monthly Notices of the Royal Astronomical Society*, 415, 2101
- Hosseini, S. M., Salmasi, B. S., Tabasi, S. S., & Firouzjaee, J. T. 2023, arXiv preprint arXiv:2306.12954
- Jiang, L., McGreer, I. D., Fan, X., et al. 2016, *The Astrophysical Journal*, 833, 222
- Karimi, N., Kazem, S., Ahmadian, D., Adibi, H., & Ballestra, L. 2020, *Engineering analysis with boundary elements*, 112, 46
- Karsoliya, S. 2012, *International Journal of Engineering Trends and Technology*, 3, 714
- Kern, N. S., Liu, A., Parsons, A. R., Mesinger, A., & Greig, B. 2017, *The Astrophysical Journal*, 848, 23
- Kim, T. 2021, arXiv preprint arXiv:2108.08186
- Kingma, D. P., & Ba, J. 2014, arXiv preprint arXiv:1412.6980
- Kosowsky, A. 2003, *New Astronomy Reviews*, 47, 939
- Liu, H., Slatyer, T. R., & Zavala, J. 2016, *Physical Review D*, 94, 063507
- Ma, Q.-B., Fiaschi, S., Ciardi, B., Busch, P., & Eide, M. B. 2022, *Monthly Notices of the Royal Astronomical Society*, 513, 1513
- Madau, P., Rees, M. J., Volonteri, M., Haardt, F., & Oh, S. P. 2004, *The Astrophysical Journal*, 604, 484
- Mapelli, M., Ferrara, A., & Pierpaoli, E. 2006, *Monthly Notices of the Royal Astronomical Society*, 369, 1719
- Meriot, R., & Semelin, B. 2023, arXiv preprint arXiv:2310.02684
- Mesinger, A., Furlanetto, S., & Cen, R. 2011, *Monthly Notices of the Royal Astronomical Society*, 411, 955
- Mesinger, A., Greig, B., & Sobacchi, E. 2016, *Monthly Notices of the Royal Astronomical Society*, 459, 2342
- Mirabel, I., Dijkstra, M., Laurent, P., Loeb, A., & Pritchard, J. 2011, *Astronomy & Astrophysics*, 528, A149
- Mitra, S., Choudhury, T. R., & Ferrara, A. 2015, *Monthly Notices of the Royal Astronomical Society: Letters*, 454, L76
- Moazzenzadeh, M., & Firouzjaee, J. T. 2021, arXiv preprint arXiv:2108.00115
- Nasir, F., & D'Aloisio, A. 2020, *Monthly Notices of the Royal Astronomical Society*, 494, 3080
- Neben, A. R., Bradley, R. F., Hewitt, J. N., et al. 2016, *The Astrophysical Journal*, 826, 199
- Ntampaka, M., Avestruz, C., Boada, S., et al. 2019, arXiv preprint arXiv:1902.10159
- Paciga, G., Albert, J. G., Bandura, K., et al. 2013, *Monthly Notices of the Royal Astronomical Society*, 433, 639
- Planck collaboration, Ade, P., Aghanim, N., et al. 2014, *A&A*, 571, A16
- Pober, J. C., Parsons, A. R., Aguirre, J. E., et al. 2013, *The Astrophysical Journal Letters*, 768, L36
- Popescu, M.-C., Balas, V. E., Perescu-Popescu, L., & Mastorakis, N. 2009, *WSEAS Transactions on Circuits and Systems*, 8, 579
- Ricotti, M. 2002, *Monthly Notices of the Royal Astronomical Society*, 336, L33
- Rohmah, M., Putra, I., Hartati, R., & Ardiantoro, L. 2021in , IOP Publishing, 012018
- Ruhl, J., Ade, P. A., Carlstrom, J. E., et al. 2004, in *Millimeter and Submillimeter Detectors for Astronomy II*, Vol. 5498, SPIE, 11–29
- Salcedo-Sanz, S., Rojo-Álvarez, J. L., Martínez-Ramón, M., & Camps-Valls, G. 2014, *Wiley Interdisciplinary Reviews: Data Mining and Knowledge Discovery*, 4, 234
- Salzo, S., & Suykens, J. A. 2020, *Analysis and Applications*, 18, 149
- Santos, M. G., Ferramacho, L., Silva, M., Amblard, A., & Cooray, A. 2010, *Monthly Notices of the Royal Astronomical Society*, 406, 2421
- Sazli, M. H. 2006, *Communications Faculty of Sciences University of Ankara Series A2-A3 Physical Sciences and Engineering*, 50
- Schmit, C. J., & Pritchard, J. R. 2018, *Monthly Notices of the Royal Astronomical Society*, 475, 1213
- Semelin, B., Eames, E., Bolgar, F., & Caillat, M. 2017, *Monthly Notices of the Royal Astronomical Society*, 472, 4508
- Shaver, P., Windhorst, R., Madau, P., & De Bruyn, A. 1999, arXiv preprint astro-ph/9901320
- Smola, A. J., & Schölkopf, B. 2004, *Statistics and computing*, 14, 199
- Sunyaev, R., & Zel'Dovich, Y. B. 1980, *Annual review of astronomy and astrophysics*, 18, 537
- Tian, Y., Shi, Y., & Liu, X. 2012, *Technological and economic development of Economy*, 18, 5
- Tingay, S. J., Goeke, R., Bowman, J. D., et al. 2013, *Publications of the Astronomical Society of Australia*, 30, e007
- Totani, T., Kawai, N., Kosugi, G., et al. 2006, *Publications of the Astronomical Society of Japan*, 58, 485
- Tripathi, A., Datta, A., Choudhury, M., & Majumdar, S. 2024, *Monthly Notices of the Royal Astronomical Society*, 528, 1945
- Van de Hulst, H. 1945, *Nederlandsch Tijdschrift voor Natuurkunde*, 11, 210
- van Haarlem, M. P., Wise, M. W., Gunst, A., et al. 2013, *Astronomy & astrophysics*, 556, A2
- Vonlanthen, P., Semelin, B., Baek, S., & Revaz, Y. 2011, *Astronomy & Astrophysics*, 532, A97
- Wang, L. 2005, *Support vector machines: theory and applications*, Vol. 177 (Springer Science & Business Media)
- Wang, W., Xu, Z., Lu, W., & Zhang, X. 2003, *Neurocomputing*, 55, 643
- Yoshida, N., Sokasian, A., Hernquist, L., & Springel, V. 2003, *The Astrophysical Journal*, 591, L1
- Zhang, H. H., Genton, M. G., & Liu, P. 2004, *Compactly supported radial basis function kernels*, Tech. rep., North Carolina State University. Dept. of Statistics